Two-dimensional supersonic plasma acceleration in a magnetic nozzle

E. Ahedo[a)] and M. Merino

ETS Ingenieros Aeronáuticos, Universidad Politécnica de Madrid, Madrid 28040, Spain

A two-dimensional model of the expansion of a collisionless, electron-magnetized, low-beta, current-free plasma in a divergent magnetic nozzle is presented. The plasma response is investigated in terms of the nozzle/plasma divergence rate, the magnetic strength on ions, and the Hall current at the nozzle throat. Axial acceleration profiles agree well with those estimated from simple one-dimensional models. A strong radial nonuniformity develops downstream. There is a separation between ion and electron/magnetic streamtubes which leads to the formation of, first, a longitudinal electric current density, which indicates that current ambipolarity is not fulfilled, and, second, a small ion azimuthal current that competes negatively with the electron azimuthal (Hall) current. The analysis of the mechanisms driving thrust, ion momentum, and ion energy unveils the dual electrothermal/electromagnetic character of the magnetic nozzle. In general, the thrust includes the contributions of volumetric and surface Hall currents, this last one formed at the plasma-vacuum interface. Plume efficiency, based on radial expansion losses, is computed. Plasma detachment and the transonic matching with the upstream plasma are not addressed. © *2010 American Institute of Physics*. [doi:10.1063/1.3442736]

I. INTRODUCTION

A guide magnetic field, created by a set of coaxial coils and forming an axisymmetric magnetic nozzle, is being used as a controlled and efficient acceleration mechanism in different plasma propulsion devices such as the applied-field magnetoplasmadynamic thruster,[1,2] the helicon thruster,[3–5] the Variable Specific Impulse Magnetoplasma Rocket (VASIMR),[6] and, marginally, in the diverging cusped field thruster.[7] Basically, these thrusters consist of the plasma source or *discharge region*, where the plasma is generated and energized, and the magnetic nozzle or *expansion region*, where nondirected plasma energy is converted into directed axial energy. Configurations similar to plasma thrusters are being used in plasma devices for advanced manufacturing and material processing.[8,9] In this case, the accelerated plasma jet impinges on the processed surface, instead of expanding indefinitely in the vacuum (with the associated problem of plasma detachment), and the main role of the nozzle is to tailor suitably the downstream plasma energy distribution; the nozzle role in a plasma thruster is to provide high specific impulse at high thrust efficiency. Plasma acceleration in a divergent magnetic field is also of interest in vacuum arc centrifuges.[10]

The similarities of a convergent-divergent magnetic nozzle with a solid Laval nozzle were studied experimentally by Andersen *et al.*,[11] who showed the subsonic/supersonic transition at the nozzle throat, where the magnetic field is maximum. A more recent experimental verification is due to Inutake *et al.*[12] Andersen *et al.* showed that their results agree with a standard one-dimensional (1D) plasma model with isothermal electrons. Inutake *et al.* estimated a specific heat ratio for electrons between 1.0 and 1.2. The 1D expansion model of Andersen *et al.* corresponds to *electrothermal*

acceleration, where plasma internal energy is converted into axial directed energy in the magnetic nozzle via the ambipolar electric field. However, plasma dynamics in a magnetic nozzle are, in general, more complex than gas dynamics in a solid nozzle because of (1) the plasma conditions upstream of the magnetic nozzle, (2) the variety of plasma acceleration mechanisms, and (3) the downstream detachment of the plasma from the guide magnetic field.

Upstream plasma conditions differ widely with the type of plasma thruster, and different types of energy deposited into the plasma lead to different acceleration mechanisms in the magnetic nozzle. Apart from the electrothermal acceleration, Sasoh[13] classified the *electromagnetic acceleration* of the plasma in three types: *Hall acceleration*, where the axial force on the plasma is due to the guiding axial magnetic field and the azimuthal electron current; *self-field acceleration*, dominant in the magnetoplasmadynamic thruster, where the axial force is created by a strong radial current and the induced azimuthal magnetic field; and *swirl acceleration*, where directed azimuthal ion energy is converted into directed axial energy by conservation of angular momentum and total energy of ions. Of course, a particular thruster can operate with more than one of these mechanisms. Furthermore, there are acceleration mechanisms not included in the preceding list, such as the *magnetic-mirror acceleration*, central in the VASIMR, where rotational energy of individual ions is converted into directed axial energy by conservation of magnetic moment and total energy of ions, and the *double-layer acceleration*, observed in some helicon thrusters,[3] where a non-neutral electric field located in the expansion region accelerates a plasma with a hot electron tail.[14,15]

Two important properties of the upstream plasma are the

---

a)Electronic mail: eduardo.ahedo@upm.es.

17, 073501-1

plasma collisionality and the thermal-to-magnetic pressure ratio (i.e., the plasma beta). For propulsion applications, the plasma in the magnetic nozzle is expected to be almost totally ionized and quasicollisionless so that plasma generation and resistivity effects can be ignored generally. However, plasmas with different ranges of beta are being tested.[5,16] The plasma beta measures the plasma capability to induce a significant magnetic self-field in the nozzle, and therefore to modify the nozzle shape, which constitutes a detachment mechanism. Once the plasma has been accelerated in the magnetic nozzle, the detachment from the magnetic lines is crucial. Otherwise, part of the plasma would turn back toward the thruster walls and the thruster efficiency would be ruined. Resistive detachment,[17] electron-inertia detachment,[18] and self-field detachment[16,19,20] are the mechanisms that have been envisaged, depending on the collisionality and beta parameter of the plasma.

Two-dimensional (2D) models of magnetic nozzles in literature are more focused in the detachment problem than in the acceleration process. Hooper[18] analyzed electron-inertia detachment with a 2D model that considers a cold, low-beta plasma, and assumes current ambipolarity (i.e., the longitudinal electric current is zero everywhere). Arefiev and Breizman[19] studied self-field detachment in a cold, high-beta plasma with an ideal magnetohydrodynamic model. Winglee *et al.*[16] applied a time-dependent, two-fluid code to analyze detachment in a collisionless, "high"-beta plasma.

This paper proposes a model of a divergent magnetic nozzle for the study of the 2D properties of the supersonic acceleration of a low-beta, collisionless plasma. After confirming that simple 1D models provide a suitable approximation of axial acceleration properties, the analysis will be focused on 2D characteristics not available to 1D models. Thus, we will discuss the influence of the nozzle divergence rate and the ion-magnetization strength (with electrons being fully magnetized always), the formation of Hall and swirl currents, the relevance of electrothermal and electromagnetic accelerations, the ratio of radial-versus-axial energy of the downstream jet, which defines the plume efficiency, the presence of surface currents at the plasma/vacuum interface and their role in thrust transmission, and the no-fulfillment of current ambipolarity, a central assumption in Hooper's model.

The layout of the rest of the paper is the following. Section II formulates the plasma/nozzle model. Section III analyzes the 2D characteristics of the plasma response. Ion magnetization and current ambipolarity are discussed in Sec. IV. Plume efficiency and the acceleration and thrust mechanisms are treated in Sec. V. Section VI summarizes the conclusions. This work is part of the theoretical contribution to an ongoing research to design a low-power helicon thruster[21] and eventually will match with a model of the upstream plasma dynamics, inside the plasma/helicon source.[22] First results on this work were presented in two recent conferences.[23,24]

II. FORMULATION OF THE MODEL

A. The magnetic nozzle

A plasma jet flows along a guide longitudinal magnetic field, $\boldsymbol{B} = B_r \boldsymbol{1}_r + B_z \boldsymbol{1}_z$. The cylindrical and magnetic reference frames are $\{\boldsymbol{1}_z, \boldsymbol{1}_r, \boldsymbol{1}_\theta\}$ and $\{\boldsymbol{b}, \boldsymbol{1}_\perp, \boldsymbol{1}_\theta\}$, with

$$\boldsymbol{b} = \boldsymbol{B}/B = \cos\alpha \boldsymbol{1}_z + \sin\alpha \boldsymbol{1}_r, \quad \boldsymbol{1}_\perp = -\sin\alpha \boldsymbol{1}_z + \cos\alpha \boldsymbol{1}_r,$$

and $\alpha(z,r)$ the local magnetic angle. The solenoidal magnetic field admits the magnetic streamfunction $\psi(z,r)$, satisfying

$$\nabla\psi = rB\boldsymbol{1}_\perp, \quad \text{i.e.,} \quad \partial\psi/\partial z = -rB_r, \quad \partial\psi/\partial r = rB_z. \tag{1}$$

This streamfunction is related to the magnetic flux across a radial section $z = z_c$, $0 \leq r \leq r_c$, through

$$2\pi \int_0^{r_c} B_z r \, dr = 2\pi\psi(z_c, r_c),$$

a magnetic streamtube is defined by $\psi(z,r) = \text{const.}$

Although our plasma/nozzle model is applicable to any divergent magnetic nozzle, for the sake of illustration, results here are presented for the nozzle created by a simple current loop of intensity I_L, flowing along $\boldsymbol{1}_\theta$, and located at $(z,r) = (0, R_L)$. (Notice that the magnetic field of more complex arrangements of current loops tends downstream to reduce to the magnetic field of a single loop.) For the single loop, the magnetic streamfunction is[25]

$$\psi(z,r) = \frac{B_0 R_L}{2\pi}\sqrt{(R_L + r)^2 + z^2}\left[(2 - k^2)\mathbf{K}(k^2) - 2\mathbf{E}(k^2)\right], \tag{2}$$

with $k^2 = 4R_L r[(R_L + r)^2 + z^2]^{-1}$, $B_0 = B_z(0,0) = \mu_0 I_L/(2R_L)$, and $\mathbf{K}(m)$ and $\mathbf{E}(m)$ the complete elliptic integrals of the first and second kind, respectively (with the argument m defined as in Ref. 26).

A current-free, fully ionized plasma jet of radius R, with $R < R_L$, is injected sonically at the nozzle throat, located at $z = 0$, and is accelerated supersonically in the divergent nozzle. The following length ordering is assumed:

$$\lambda_d \ll \ell_e \ll R_V \ll \lambda_c, \tag{3}$$

with λ_d as the Debye length, ℓ_e as the electron gyroradius, λ_c as the electron-ion collision mean-free path, and $R_V(z)$ as the jet cross-section radius along the nozzle. That ordering implies that (1) plasma quasineutrality holds everywhere, (2) the plasma is treated as collisionless, and (3) electrons are fully magnetized and the streamtubes for massless electrons are the magnetic streamtubes. Furthermore, because of quasineutrality and magnetic guiding of electrons, the edge V of the plasma jet (i.e., the plasma-vacuum transition) is the magnetic streamsurface that develops from the cross section of radius R at the throat, that is, $r = R_V(z)$, with $R_V(z)$ defined implicitly by

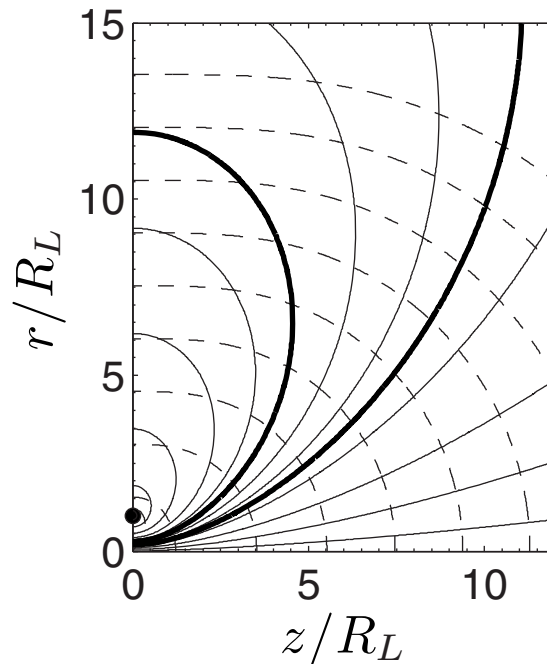|	Low-beta plasma[a]	"High"-beta plasma[b]
B_0 (G)	1000	200
n_0 (m^{-3})	7×10^{18}	2×10^{19}
R (mm)	10	100
T_e (eV)	20	20
c_e (m/s)	1.9×10^6	1.9×10^6
c_s (m/s)	6.9×10^3	6.9×10^3
c_{a0} (m/s)	1.3×10^5	1.5×10^4
λ_{d0} (mm)	1.3×10^{-2}	7.3×10^{-3}
ℓ_{e0} (mm)	0.11	0.53
$\hat{\Omega}_{i0} \equiv R\Omega_{i0}/c_s$	0.35	0.70
$\beta = c_s^2/c_{a0}^2$	2.8×10^{-3}	0.2
ℓ_{e0}/R	1.1×10^{-2}	5.3×10^{-3}
λ_{d0}/R	1.3×10^{-3}	7.3×10^{-4}

[a]Reference 5.
[b]Reference 16.

FIG. 1. Solid lines are the magnetic streamlines created by a circular ring located at $r = R_L$ and $z = 0$ (black circle). Dashed lines are the constant-B lines. The thick solid lines correspond to the two nozzles (i.e., plasma jet edges) used in the simulations: $R_L/R = 3.5$ (short nozzle) and 5.4 (long nozzle). The turning points of these nozzles are at $(z,r)/R \approx (16,22)$ and $(60,85)$, respectively.

$$\psi[z, R_V(z)] = \psi(0, R).$$

Equation (3) states that the magnetic strength is large enough to guide the electrons but it does not inform on ion magnetization. We will consider the general case

$$R\Omega_{i0}/u_{i0} = O(1), \tag{4}$$

where subscript 0 refers always to the nozzle throat, $\Omega_i = eB/m_i$ is the local ion gyrofrequency, and u_i is the macroscopic ion velocity. Except for $R\Omega_{i0}/u_{i0} \to \infty$, ion streamtubes are not going to coincide with magnetic/electron streamtubes. The low-beta plasma assumption is

$$\beta_0 = c_{s0}^2/c_{a0}^2 \ll 1, \tag{5}$$

with c_s as the sound velocity and c_a as the Alfvén velocity (based on the guide field). Condition (5) tries to ensure that the induced magnetic field $\boldsymbol{B}^*$ can be neglected, i.e., $B^* \ll B$. Finally, the plasma is considered current-free so that the electric current across any radial section of the external streamtube V is zero,

$$I(z) = \int_{A_V(z)} dA j_z = 0. \tag{6}$$

Here, $A_V(z) = \pi R_V^2(z)$ is the plasma jet radius at z and j_z is the axial component of the electric current density $\boldsymbol{j}$.

Table I details plasma parameters based on experimental values from two helicon thruster sources. Figure 1 plots the magnetic streamlines for a simple loop and the edges of two plasma jets used in the simulations here. If the plasma radius and properties are fixed, the magnetic nozzle is characterized by its shape and strength parameters, R_L/R and $R\Omega_{i0}/u_{i0}$, respectively. An optimization of the magnetic nozzle requires an investigation of the influence of these two parameters. In principle, low-divergence nozzles (i.e., R_L/R large) seem favorable since the nozzle turning point (i.e., the point where $B_z = 0$) is further downstream and sidestream. However, for R and B_0 given, R_L/R is limited by the electric power and the

weight of the current loop. These scale as $R_L^3 A_L^{-1}$ and $R_L A_L$, respectively, with A_L as the total cross section of the current loop.

B. General plasma equations

Macroscopic, steady-state equations for a species j of a collisionless plasma are

$$\nabla \cdot n_j \boldsymbol{u}_j = 0, \tag{7}$$

$$m_j n_j \boldsymbol{u}_j \cdot \nabla \boldsymbol{u}_j = -\nabla n_j T_j - q_j n_j \nabla \phi + q_j n_j \boldsymbol{u}_j \times \boldsymbol{B}, \tag{8}$$

where q_j is the electric charge, ϕ is the ambipolar electric potential, and the rest of symbols are conventional. These equations are to be completed by energy or state equations for T_j.

For our axisymmetric problem (i.e., $\partial/\partial\theta = 0$), it is convenient to decompose vectorial magnitudes into longitudinal and azimuthal components. For instance, for the velocity, we write

$$\boldsymbol{u}_j = \tilde{\boldsymbol{u}}_j + u_{\theta j} \boldsymbol{1}_\theta, \tag{9}$$

with $\tilde{\boldsymbol{u}}_j \cdot \boldsymbol{1}_\theta = 0$. The longitudinal velocity $\tilde{\boldsymbol{u}}_j$ admits a streamfunction $\psi_j(z,r)$, which satisfies

$$\partial\psi_j/\partial z = -rnu_{rj}, \quad \partial\psi_j/\partial r = rnu_{zj}. \tag{10}$$

Making use of the axisymmetry and the velocity decomposition, Eqs. (7) and (8) become

$$\nabla \cdot n_j \tilde{\boldsymbol{u}}_j = 0, \tag{11}$$

$$r^{-1} \tilde{\boldsymbol{u}}_j \cdot \nabla(rm_j u_{\theta j}) = q_j(\tilde{\boldsymbol{u}}_j \times \boldsymbol{B}) \cdot \boldsymbol{1}_\theta, \tag{12}$$

$$m_j \tilde{\boldsymbol{u}}_j \cdot \nabla \tilde{\boldsymbol{u}}_j = -\nabla(h_j + q_j\phi) + \mathbf{1}_\perp q_j u_{\theta j}B + \mathbf{1}_r m_j u_{\theta j}^2/r, \quad (13)$$

where $h_j \equiv n_j^{-1}\nabla p_j$ is the barotropic function and $\tilde{\boldsymbol{u}}_j \cdot \nabla$ is the derivative along the (meridian-projected) streamlines. From Eq. (1), one has

$$\tilde{\boldsymbol{u}}_j \times \boldsymbol{B} \cdot \mathbf{1}_\theta = -r^{-1}\tilde{\boldsymbol{u}}_j \cdot \nabla\psi, \quad (14)$$

which, substituted into Eq. (12), leads to the conservation of the total angular momentum of species j along a streamline,[18]

$$rm_j u_{\theta j} + q_j\psi = D(\psi_j), \quad (15)$$

with $D(\psi_j)$ determined from entrance conditions.

Using this last equation, Eq. (13) becomes

$$m_j \tilde{\boldsymbol{u}}_j \cdot \nabla \tilde{\boldsymbol{u}}_j = -\nabla(h_j + q_j\phi + m_j u_{\theta j}^2/2) + r^{-1}u_{\theta j}\nabla D(\psi_j). \quad (16)$$

The projection of Eq. (16) along a streamtube yields the conservation of the Bernoulli function along the streamtube,

$$h_j + q_j\phi + m_j u_j^2/2 = H(\psi_j). \quad (17)$$

Incidentally, Eq. (11) of Hooper[18] should correspond to the case $h_j = 0$ of Eq. (16) but Hooper missed the last term, $r^{-1}u_{\theta j}\nabla D(\psi_j)$. Hence, his model is valid only for entrance conditions satisfying $D(\psi_j) = \text{const}$.

C. Plasma model

For a current-free plasma, electrons are confined by the ambipolar electric field and only a very small fraction of them flows downstream to neutralize the ion beam. Therefore, occasional collisions ultimately thermalize the confined electron population leading to $T_e = \text{const}$. Ion pressure will be neglected (i.e., $T_i \ll T_e$) since it is smaller than the electron pressure (commonly) and the dynamic ion pressure (for a supersonic flow). Ions are assumed singly charged and electron inertia is neglected. Applying these additional assumptions to the preceding general plasma equations, the plasma model consists of

$$\nabla \cdot n\tilde{\boldsymbol{u}}_i = 0, \quad (18)$$

$$m_i \tilde{\boldsymbol{u}}_i \cdot \nabla \tilde{\boldsymbol{u}}_i = -e\,\nabla\,\phi + \mathbf{1}_\perp e u_{\theta i}B + \mathbf{1}_r m_i u_{\theta i}^2/r, \quad (19)$$

$$rm_i u_{\theta i} + e\psi = D_i(\psi_i), \quad (20)$$

$$\tilde{\boldsymbol{u}}_e = u_{\|e}\boldsymbol{b}, \quad (21)$$

$$nu_{\|e}/B = G_e(\psi), \quad (22)$$

$$0 = -T_e\,\nabla\,\ln n + e\,\nabla\,\phi - e u_{\theta e}B\mathbf{1}_\perp, \quad (23)$$

which is a closed set for determining n, ϕ, $\boldsymbol{u}_i$, and $\boldsymbol{u}_e$. Equations (20) and (22) can be seen as algebraic equations for $u_{\theta i}$ and $u_{\|e}$; D_i is the ion total angular momentum and G_e is the ratio of electron-to-magnetic flux in each electron/magnetic streamtube.

The two components of the electron momentum equation (23) yield two algebraic equations for ϕ and $u_{\theta e}$,

$$T_e \ln n - e\phi = H_e(\psi), \quad (24)$$

$$u_{\theta e} = -\frac{1}{eB}\frac{\partial H_e}{\partial \mathbf{1}_\perp} = -\frac{r}{e}\frac{dH_e}{d\psi}. \quad (25)$$

Here, $T_e \ln n$ is the barotropic function of the electron gas and $H_e(\psi)$ is the electron Bernoulli function. There are two interpretations for each one of Eqs. (24) and (25). In the first one, Eq. (24) is a generalized Boltzmann relation, with $-H_e/e$ as the thermalized potential, and Eq. (25) states that the electron azimuthal velocity is a B-perpendicular drift, with contributions of both the electric field and the pressure gradient. In the second interpretation, Eqs. (24) and (25) establish the conservation of two electron magnitudes in each streamtube: the Bernoulli function and the azimuthal frequency $u_{\theta e}/r$. An important consequence of the last conservation law is that if the electron flow does not rotate initially (i.e., at the nozzle throat), there is no mechanism in this collisionless plasma to put it into rotation downstream. Since the magnetic streamtubes diverge, Eq. (18) says that the electron azimuthal velocity increases downstream the nozzle.

The ion and electron current densities, $\boldsymbol{j}_i = en\boldsymbol{u}_i$ and $\boldsymbol{j}_e = -en\boldsymbol{u}_e$, and the resultant electric current density, $\boldsymbol{j} = \boldsymbol{j}_i + \boldsymbol{j}_e$, are important magnitudes in the plasma response. For convenience, they are split into longitudinal and azimuthal components in the same way than $\boldsymbol{u}_j$ in Eq. (9). Following the notation of Sasoh,[13] $j_{\theta e}$ and $j_{\theta i}$ will be referred to as *Hall and swirl currents*, respectively. As seen in Eq. (25), a Hall current is the resultant of the $E \times B$ and diamagnetic drifts on electrons. This is not the case for the swirl current: since ion motion in Eq. (19) is dominated by inertia, the development of a swirl current (resulting in a rotating plasma) is governed by the conservation of total angular momentum in Eq. (20), instead of by the $E \times B$ drift.

D. Numerical integration and throat conditions

Adding Eqs. (19) and (23) in order to eliminate the electric field, the three differential equations for n and $\tilde{\boldsymbol{u}}_i$ can be expressed as

$$u_{ri}\frac{\partial \ln n}{\partial r} + u_{zi}\frac{\partial \ln n}{\partial z} + \frac{\partial u_{ri}}{\partial r} + \frac{\partial u_{zi}}{\partial z} = -\frac{u_{ri}}{r}, \quad (26)$$

$$u_{ri}\frac{\partial u_{ri}}{\partial r} + u_{zi}\frac{\partial u_{ri}}{\partial z} + c_s^2\frac{\partial \ln n}{\partial r} = -(u_{\theta e} - u_{\theta i})\Omega_i \cos\alpha + \frac{u_{\theta i}^2}{r}, \quad (27)$$

$$u_{ri}\frac{\partial u_{zi}}{\partial r} + u_{zi}\frac{\partial u_{zi}}{\partial z} + c_s^2\frac{\partial \ln n}{\partial z} = (u_{\theta e} - u_{\theta i})\Omega_i \sin\alpha, \quad (28)$$

with $c_s = \sqrt{T_e/m_i}$. These three equations, coupled to the algebraic equations for the rest of variables, are integrated numerically with the method of characteristics,[27] detailed in Appendix A. Prior to integration, the energy T_e, the sound speed c_s, the length R, and the density $n_0 = n(0,0)$ are used to nondimensionalize all plasma magnitudes, and dimensionless variables are expressed with a hat: $\hat{n} = n/n_0$, $\hat{\phi} = e\phi/T_e$, etc. The plasma Mach number is defined from the ion longitudinal velocity: $M = \tilde{u}_i/c_s$.

In order to integrate the equations and once the tube V has been imposed as the plasma edge, the plasma state at the nozzle throat remains to be defined. This depends very much on the plasma source located upstream of the nozzle (i.e., on the particular thruster type). Here we will focus on two plasma types. One of them would idealize the plasma jet exiting a magnetized cylindrical vessel with no internal electrodes, as in a helicon-plasma source.[22,28] This plasma is current-free, has negligible rotation, and a strong Hall current that balances a strong radial gradient of plasma density. Appendix B summarizes the main characteristics of this plasma at the exit of the vessel, which define the nozzle entrance conditions below. The second plasma type corresponds to the zero Hall-current limit of the first one. The two plasmas will be called *nonuniform* and *uniform* plasma jets (although both of them are obviously nonuniform downstream).

The throat conditions consistent with these two plasma types and the model equations are

$$\hat{u}_{zi} = M_0 \simeq 1, \tag{29}$$

$$\hat{u}_{ze} = \hat{u}_{zi}, \tag{30}$$

$$\hat{u}_{ri} = \hat{u}_{re} = 0, \tag{31}$$

$$\hat{\phi} = 0, \tag{32}$$

$$\hat{n} = J_0(a_0 \sigma \hat{r}), \tag{33}$$

$$\hat{j}_{\theta e} = -\hat{\Omega}_{i0}^{-1} a_0 J_1(a_0 \sigma \hat{r}), \quad \hat{u}_{\theta e} = -\hat{j}_{\theta e}/\hat{n}, \tag{34}$$

$$\hat{u}_{\theta i} = 0, \tag{35}$$

at $\hat{z}=0$ and $0 \leq \hat{r} \leq 1$. Here, M_0 is the plasma Mach number at the entrance; the dimensionless gyrofrequency, $\hat{\Omega}_{i0} = eB_0 R / m_i c_s$, measures the ion magnetization strength at the throat, J_0 and J_1 are Bessel functions of the first kind, with $a_0 = 2.405$ the first zero of J_0, and the parameter σ measures both the Hall current and the radial nonuniformity of the plasma density. The two distinguished cases are $\sigma=0$ for the uniform jet and $1 - \sigma \ll 1$ for the nonuniform jet.

Figure 2 plots radial profiles at the throat for the nonuniform jet. Both the plasma density and the Hall current density present smooth radial variations. This makes $\hat{u}_{\theta e}(r) \sim 1$ except very near the jet edge, where the small value of $n(0,R)$ produces a large steepening of the azimuthal velocity up to $\hat{u}_{\theta e}(0,R) \approx [(1-\sigma)\hat{\Omega}_{i0}]^{-1}$. Notice from Eq. (25) that $\hat{u}_{\theta e}/\hat{r}$ at $\hat{z}=0$ measures $dH_e/d\psi$. The Hall current density at the edge is $\hat{j}_{\theta e}(0,R) \simeq -\hat{\Omega}_{i0}^{-1} a_0 J_1(a_0) \simeq -1.25 \hat{\Omega}_{i0}^{-1}$.

Condition (31) is compatible with Eq. (32) and $B_r=0$, and conditions (31)–(33) are compatible with electron equations (24) and (25). Condition (30) means that current ambipolarity is satisfied at the throat, i.e., $\tilde{J}_z(0,r)=0$, and assures that the plasma jet is going to be current-free everywhere, i.e., $I(z)=0$ in Eq. (6). [Solutions with $\tilde{J}_z(0,r) \neq 0$ in a current-free plasma will be commented on in Sec. IV.] The radial distribution of the ion flow is $2\pi\psi_i$ [Fig. 2(d)]. Only at
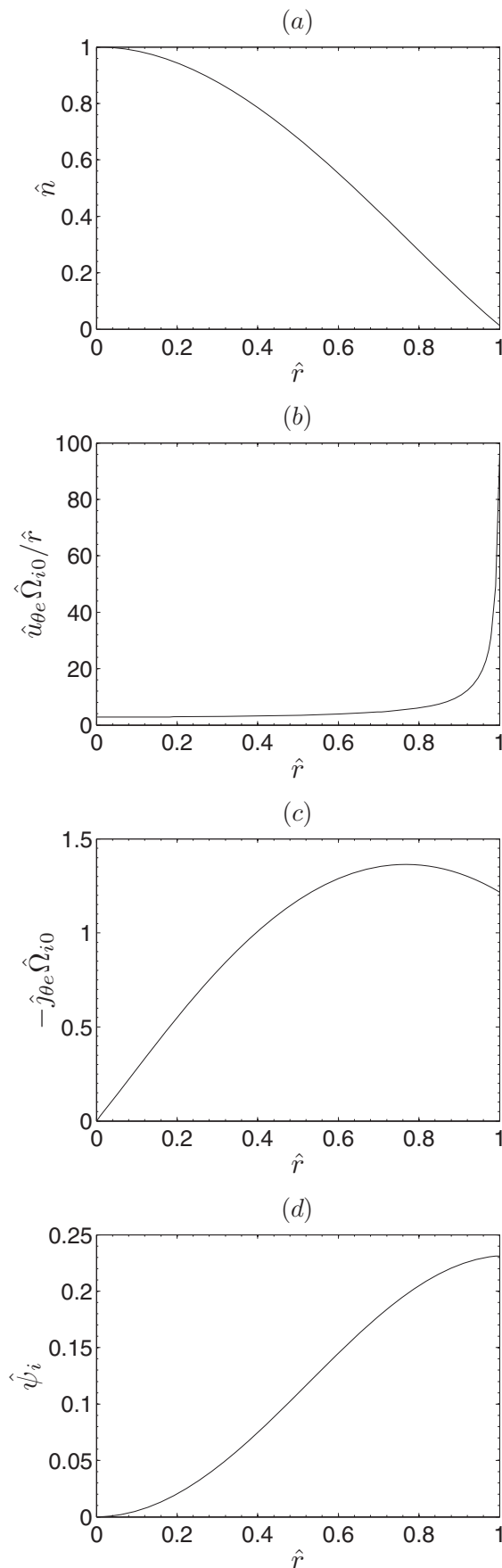

FIG. 2. Radial profiles of dimensionless plasma magnitudes at the nozzle throat, $z=0$, for a nonuniform jet with $\sigma=0.99$. (a) Plasma density, (b) azimuthal electron frequency, (c) azimuthal electron current density, and (d) ion flux nondimensionalized as $\hat{\psi}_i = \psi_i/(R^2 n_0 c_s)$.

the throat the electron flow distribution, $2\pi\psi_e$, coincides with the ion flow distribution. Since $B(0,r)\simeq$ const for R_L/R large, the magnetic flow distribution at the throat is $2\pi\psi(0,r)\simeq\pi B_0 r^2$.

The throat conditions contain all the information needed to determine the four conserved magnitudes, $D_i(\psi)$, $G_e(\psi)$, $H_e(\psi)$, and $dH_e/d\psi$, on the algebraic equations for $u_{\theta i}$, $u_{\|e}$, ϕ, and $u_{\theta e}$. Then, the differential equations are integrated from $z=0$ to a downstream location $z=z_F$, located near the turning point of the selected nozzle (Fig. 1). Since $M_0=1$ is not admitted by the integration scheme, a value of $M_0=1.05$ is chosen in most simulations. Certainly, this yields a local error. A more correct procedure would be to apply Sauer's method or a similar one to determine the sonic surface [i.e., $M(z,r)=1$] and the local plasma expansion around it.[27] This task is not afforded here because, first, we are interested in the whole plasma acceleration process and not in the transonic flow characteristics around the nozzle throat, and second, it would require to define in more detail the subsonic model of the plasma at the convergent side of the throat. Of course, we expect errors related to the small parameter (M_0-1) to be small except in the throat neighborhood; this is checked at the end of Sec. V.

For $M_0\simeq1$, three dimensionless parameters characterize the solution: $\hat{\Omega}_{i0}$ for the ion-magnetization strength, σ for the jet initial nonuniformity, and R_L/R, which measures the divergence rate of the nozzle. Most results in the next sections involve three ion magnetization strengths, $\hat{\Omega}_{i0}=0.1$, 10, and 100, a uniform jet ($\sigma=0$) and a highly nonuniform jet (with $\sigma=0.99$), and the short and long nozzles depicted in Fig. 1. Downstream, the integration ends at $\hat{z}_F=14$ and 56 for the short and long nozzles, respectively. The respective area expansion ratios of these nozzles are 177 and 3435; the long nozzle reaches an area expansion of 177 at $\hat{z}\simeq26.7$.

III. AXIAL AND RADIAL EXPANSION

Figures 3(a)–3(c) show the axial variation in the main variables at the axis and edge of the uniform jet. The difference between the values at these two streamtubes measures the radial nonuniformity that develops downstream. Contrary to the case of an adiabatic gas, where the pressure and the sound speed decrease quickly along the nozzle and the flow becomes soon hypersonic, in this isothermal plasma the electron pressure does not vanish and the Mach number increases gently, which agrees with experimental results.[11,12]

Taking into account that the expansion ratio for the long nozzle is above 10^3, the radial nonuniformity of the jet at z_F is large for the density but mild for the potential and the kinetic energy. This suggests that a simple 1D nozzle model may provide a good approximation of the axial plasma acceleration. The 1D model equations are[11,15]

$$\hat{R}_V^2(\hat{z})\bar{n}\bar{M}=M_0, \quad \bar{n}=e^{\bar{\phi}}, \quad \bar{M}=\sqrt{M_0^2-2\bar{\phi}}, \tag{36}$$

where $\bar{n}(\hat{z})$, $\bar{M}(\hat{z})$, and $\bar{\phi}(\hat{z})$ represent dimensionless, r-averaged variables. The potential profile, $\bar{\phi}(\hat{z})$, is obtained from the implicit equation
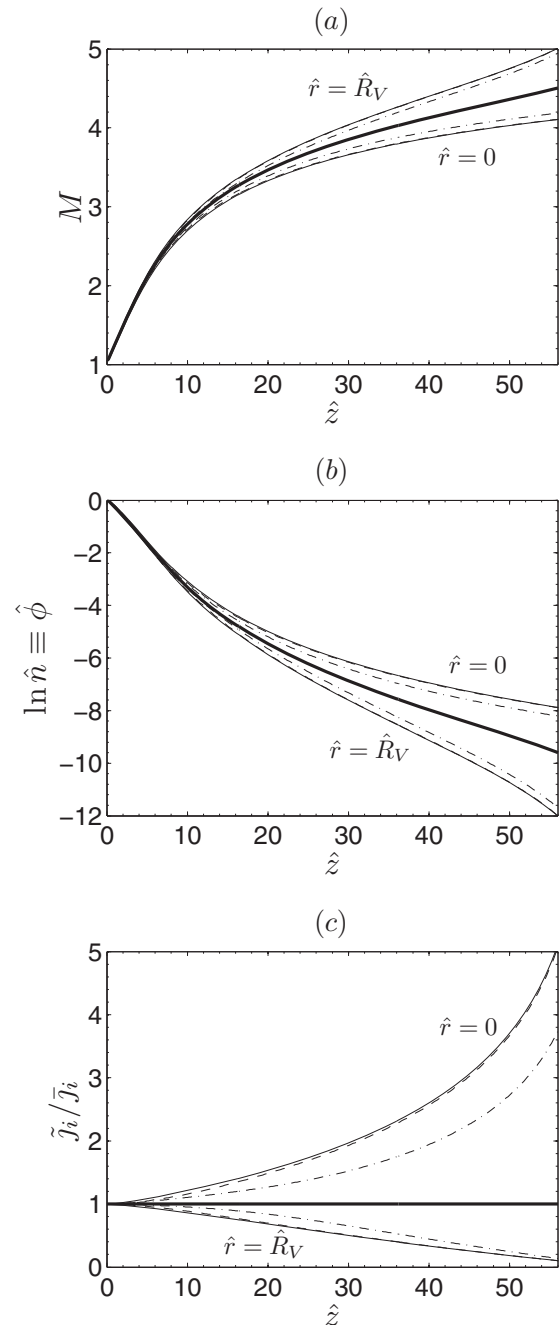

FIG. 3. Axial evolution of dimensionless magnitudes of the uniform jet ($\sigma=0$) in the long nozzle for $\hat{\Omega}_{i0}=0.1$ (solid lines), 10 (dashed lines), and 100 (dashed-dotted lines). (a) Plasma Mach number, (b) electric potential, and (c) ion longitudinal current over r-averaged value, $\bar{J}_i(z)=I_i/\pi R_V^2(z)$. The thick lines correspond to the solution of the 1D model [Eqs. (36) and (37)]. Lines $r=0$ and $r=R_V$ (at different sides of the thick lines) correspond to the jet axis and edge, respectively.

$$\hat{R}_V^2(\hat{z})e^{\bar{\phi}}\sqrt{M_0^2-2\bar{\phi}}=M_0, \tag{37}$$

and the averaged ion (and electron) current density is $\bar{J}_i(z)=I_i/\pi R_V^2(z)$. The results for the 1D model, also plotted in Fig. 3, confirm that it approximates well the axial acceleration process. For the rest of the features of the plasma response, the 2D model is necessary. In particular, Fig. 3(c) shows that the relative ion flux does not remain uniform radially and tends to concentrate around the axis as the plasma moves

downstream (which is going to be beneficial for both plasma detachment and thrust efficiency).

Figures 4(a)–4(d) show, for the same nozzle, the expansion of the highly nonuniform jet. Interestingly, the axial acceleration profiles are very similar to the case of the uniform jet; both the radial electric field and the Mach number at the edge are a bit larger now [Figs. 4(a) and 4(b)]. Therefore, the 1D model provides again a good estimate of the axial jet expansion. A prominent 2D feature is the increasing radial nonuniformity of the plasma density, shown both in Figs. 4(c) and 4(d). Although the jet expands with the nozzle, the radial electric field tends to confine further the plasma, explaining the steepening of the radial shape of $\hat{n}$ in Fig. 4(d). Equation (25) suggests that $u_{\theta e}$ preserves approximately its radial shape. Then, the gentle maximum of the radial shape $j_{\theta e}(r)$ at the throat [Fig. 2(c)] tends to shift toward the axis and to become more pronounced downstream.

The validity of our plasma/nozzle model relies on the length ordering of Eq. (3). Since plasma properties change widely along the nozzle, it is not enough that Eq. (3) is satisfied at the throat. In other words, we must check whether the two basic assumptions of the model, plasma quasineutrality and magnetic guiding of the electron (measured by λ_d/R_V and ℓ_e/R_V, respectively), are well satisfied until the final section z_F. Figures 5(a) and 5(b) plot the evolution of these two ratios along the nozzle. The wide hats on λ_d/R_V and ℓ_e/R_V mean that they are values relative to those at the throat (which can be estimated in Table I for two particular cases). The two relative ratios are more critical at the jet edge. The growth of the electron gyroradius ratio is estimated as $\ell_e/R_V \propto R_V^{-1}B^{-1} \propto R_V$. The growth of the Debye-length ratio is $\lambda_d/R_V \propto R_V^{-1}n^{-1/2} \propto M^{1/2}$ near the throat, but downstream it increases faster because of the additional radial rarefaction of the plasma [Fig. 4(d)]. For the plasma values of Table I and our simulation cases, plasma quasineutrality and magnetic guiding of electrons are well preserved until $z=z_F$.

IV. MAGNETIZATION STRENGTH AND CURRENT AMBIPOLARITY

The magnetization strength on ions is measured by the parameter $\hat{\Omega}_{i0}$. The extrapolation of the examples of Table I suggests that the range $\hat{\Omega}_{i0} \leq O(10)$ covers most applications. Because of the nozzle divergence, the *local* magnetization parameter,

$$\frac{\Omega_i R_V}{u_i} \sim \frac{\hat{\Omega}_{i0}}{\hat{R}_V M}, \tag{38}$$

decays along the nozzle and so does ion magnetization. Thus, the ion flow can be considered magnetized only within the region $\hat{\Omega}_{i0} > \hat{R}_V(z)M(z) \geq 1$. As a consequence, in the practical range $\hat{\Omega}_{i0} \leq O(10)$, the effects of ion magnetization on both the axial and the radial expansion of the plasma are rather weak, as Figs. 3 and 4 illustrate.

The fact that ions are partially magnetized while electrons are fully magnetized sets up interesting phenomena (not reproducible by a 1D model). On the one hand, elec-
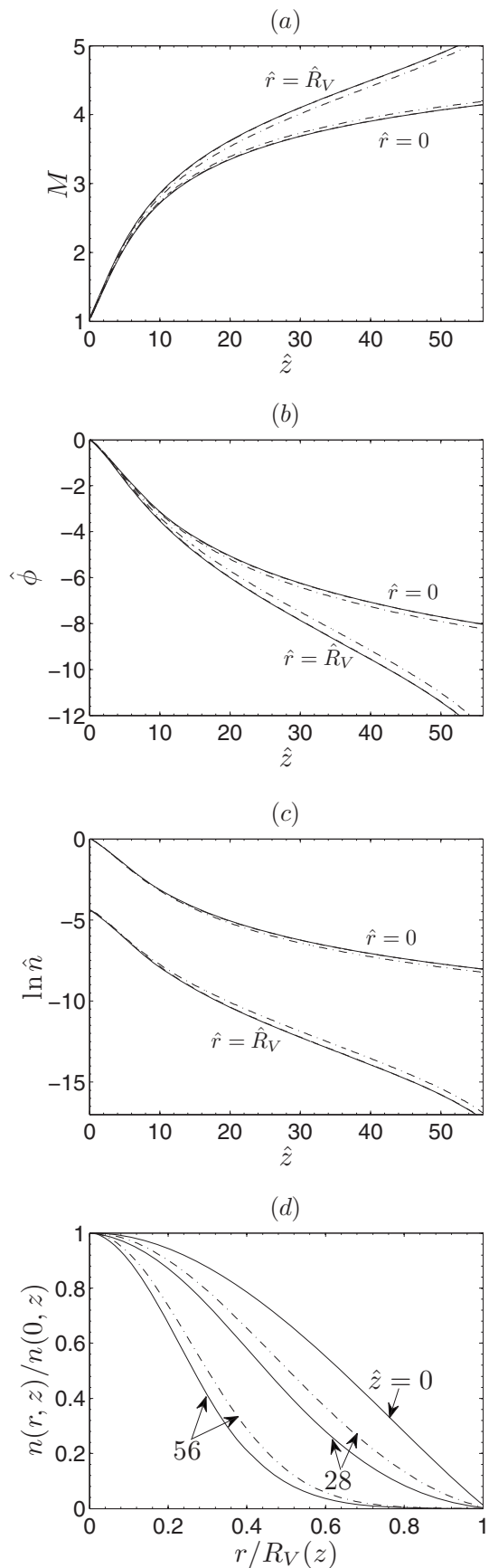

FIG. 4. Axial evolution of (a) the ion longitudinal velocity, (b) the electric potential, and (c) the logarithm of plasma density for the nonuniform jet ($\sigma=0.99$) in the long nozzle. In (d) normalized radial profile of plasma density at three axial locations. Solid, dashed, and dash-and-dot lines are for $\hat{\Omega}_{i0}=0.1$, 10, and 100, respectively.

(a)

(a)

(b)

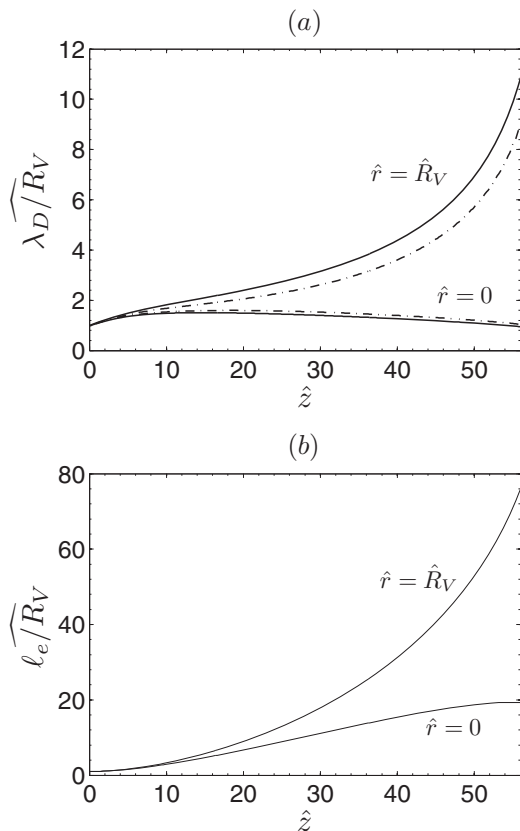$\hat{\Omega}_{i0} = 0.1$

$\hat{\Omega}_{i0} = 100$

(b)

FIG. 5. Variation in the (a) quasineutrality and (b) electron-guiding parameters for the long nozzle and $\hat{\Omega}_{i0}=0.1$ (solid lines), 10 (dashed lines), and 100 (dashed-dotted lines). The two parameters are normalized with their values at $z=0$.

(c)

(d)

trons are forced to lie within the magnetic streamtubes because of the dominant magnetic confinement. On the other hand and according to Eq. (19), ions, if weakly magnetized, are driven by the ambipolar electric field, which is self-adjusted by plasma quasineutrality. Then, the radial expansion of the ion streamtubes is governed by the radial electric field. Figure 6(a) shows that the divergence of the ion streamtubes is lower than the divergence of the electron/magnetic streamtubes (except, of course, at the edge of the plasma jet). As ion magnetization increases, there is an additional ion radial expansion caused by $u_{\theta i}B$, but the comparison of Figs. 6(a) and 6(b), with $\hat{\Omega}_{i0}$ differing in three orders of magnitude, shows that the radial magnetic force is small compared to the electric one. Only in the asymptotic limit $\hat{\Omega}_{i0} \rightarrow \infty$ ion and magnetic streamtubes would coincide, but the present analysis shows that that asymptotic limit is not a good approximation for partial magnetization, even for $\hat{\Omega}_{i0} \sim 100$, already a too large value for practical devices.

Since the ion fluid is cold and the model stationary, the trajectories of individual ions are indeed the ion streamlines, which, for $u_{\theta i} \neq 0$, are helicoidal with respect to the nozzle axis; the streamtube shapes of Figs. 6(a) and 6(b) represent the projection of the streamlines on the meridian plane. Indeed, the accuracy of our integration scheme has been confirmed by checking that the ion streamlines agree with ion trajectories computed using the electric field yielded by the
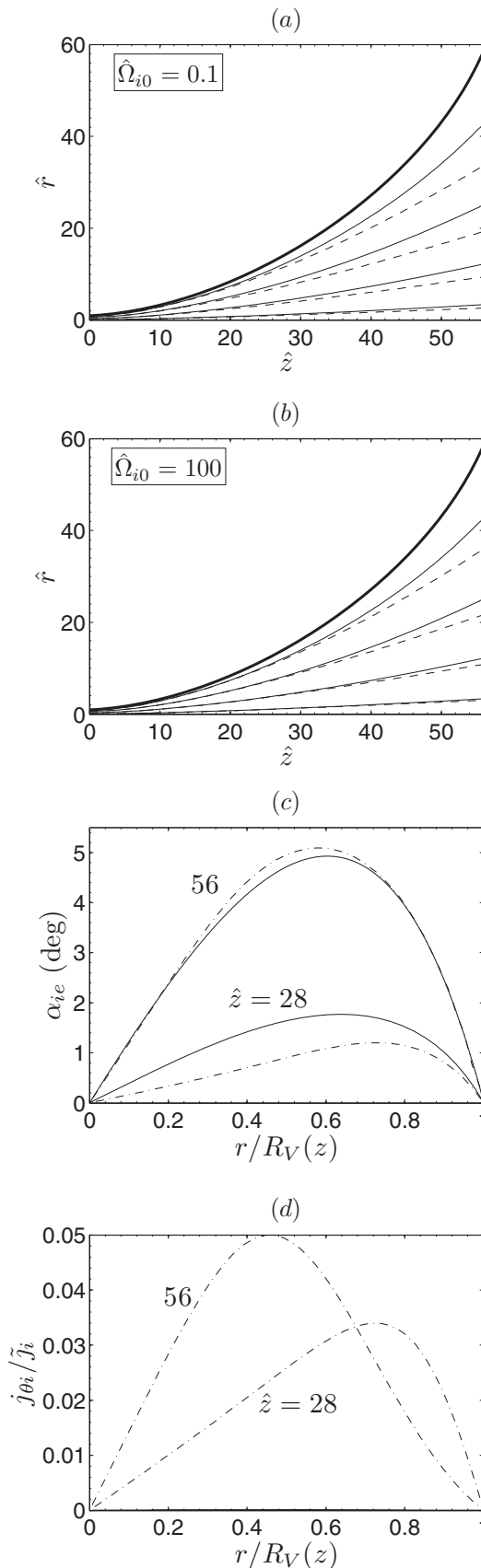
FIG. 6. [(a) and (b)] Magnetic/electron (solid) and ion (dashed) streamtubes with the same initial cross section and two magnetic strengths. Curves are for the uniform jet and the long nozzle. (c) Local separation angle between ion-electron streamtubes and (d) swirl current for $\hat{\Omega}_{i0}=0.1$ (solid) and 100 (dashed-dotted) at two axial locations; the solid lines in (d) are undistinguishable from the abscissa axis.

macroscopic integration scheme. If the ion fluid was not "cold" and ion pressure (i.e., velocity dispersion c_i in the collisionless case) was included, ion gyromotion and the subsequent effects of a finite Larmor radius, $\ell_i = c_i/\Omega_i$, should be taken into account. These effects vanish for full and weak magnetization. In a divergent, decreasing magnetic field they would matter only in the limited nozzle region where ℓ_i is small but of the order of the jet radius.

Figure 6(c) plots the *local* separation angle, $\alpha_{ei} = \text{angle}(\tilde{u}_i, \tilde{u}_e)$, between ion and electron streamtubes for two ion-magnetization strengths. For $\hat{\Omega}_{i0}$ finite, the separation angle is quite modest but it is at the base of the generation of electric currents in the plasma jet. First, it creates a swirl current, $j_{\theta i}$, in the initially nonrotating plasma, which is plotted in Fig. 6(d). According to Eq. (12), one has $u_{\theta i} \sim \Omega_i R_V \sin \alpha_{ei}$. Since $u_{\theta e}$ and $u_{\theta i}$ are positive the swirl current runs *opposite* the Hall current. The plasma swirling created in the nozzle is small compared to the longitudinal ion current,

$$\frac{j_{\theta i}}{\tilde{J}_i} \sim \frac{\Omega_i R_V}{u_i} \sin \alpha_{ei} \ll 1, \tag{39}$$

but, as we will see below, it can have a non-negligible, negative effect on the performances of the plasma-nozzle system.

Second, the small ion-electron streamtube separation has a cumulative effect on the relative cross sections of a pair of ion and electron streamtubes with the same cross section at the throat. At a distance z from the throat, the difference in the cross-section radius of the two streamtubes becomes $O(z \sin \alpha_{ei})$, with the ion streamtube having the smallest cross section. Since a pair of these streamtubes transport a constant and equal current of ions and electrons, their progressive separation implies that the electron current contained in the (less divergent) ion streamtube is lower than the ion current. Therefore, a positive axial electric current develops in the central part of the jet and, since the plasma is current-free, a negative axial electric current is found in the vicinity of the jet edge. Figure 7(a) shows the axial and radial development of the longitudinal electric current density, *relative* to the longitudinal ion current density. Figure 7(b) shows the radial variation in the relative axial electric current density j_z, and Fig. 7(c) depicts the electric current density lines. The relative electron-to-ion current becomes quite large near the jet edge but, since $\tilde{J}_i$ decreases proportionally to the nozzle area, $\tilde{J}$ tends to vanish downstream. As expected, the electric current density decreases as ion magnetization increases but it is still well observable in Fig. 7(a) for $\hat{\Omega}_{i0} = 100$.

The development of electric currents in the plasma means that, for $\hat{\Omega}_{i0}$ finite, current ambipolarity (i.e., $\tilde{J} = 0$) is satisfied *only* at a particular transverse section of the plasma jet. Condition (30) sets $\tilde{J} = 0$ at the nozzle throat, but solutions are immediate for other cases of a current-free plasma, i.e., with $\int_0^1 \tilde{J}_z(0, \hat{r}) = 0$. To understand this, observe that the computations of $u_{\|e}$ [Eq. (22)] and $\tilde{J}_e(\hat{z}, \hat{r}) = -en u_{\|e} \boldsymbol{b}$ are carried out after solving the rest of equations. Therefore, the modification of condition (30) is not going to change the
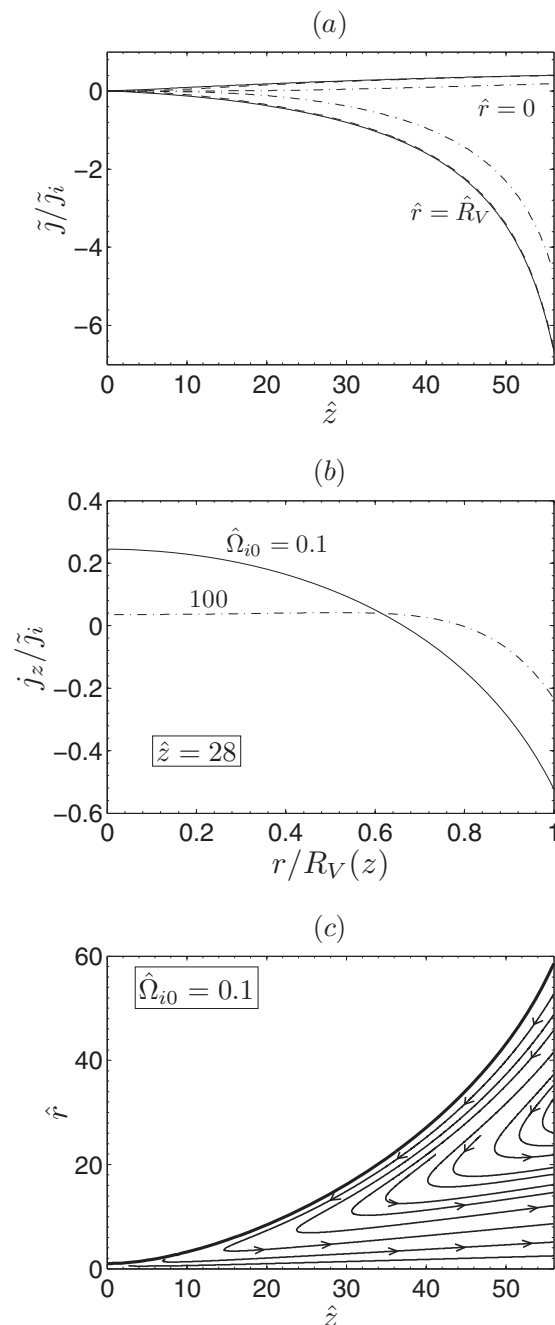

FIG. 7. (a) Longitudinal electric current density at the jet axis and edge for $\hat{\Omega}_{i0} = 0.1$ (solid), 10 (dashed), and 100 (dashed-dotted). (b) Axial electric current density at $\hat{z} = 28$ for $\hat{\Omega}_{i0} = 0.1$ and 100. (c) Map of electric current density lines for $\hat{\Omega}_{i0} = 0.1$. Results are for the long nozzle and the uniform jet (with current ambipolarity, $\tilde{J} = \boldsymbol{0}$, imposed at the throat).

plasma acceleration response, only the profiles of $\tilde{J}_e(\hat{z}, \hat{r})$ and $\tilde{J}(\hat{z}, \hat{r})$. As an example, Fig. 8 plots the electric current density when current ambipolarity is imposed at the integration final section, $\tilde{J}_z(z_F, r) = 0$, keeping the rest of conditions as in Fig. 7. The patterns are the same in both figures except that, in Fig. 8, the electric current density has the opposite sign and grows upstream instead of downstream.

In fact, the case of Fig. 8 seems a good simulation of the real application of a plasma/nozzle device for material processing[9] when the plasma jet impacts on a floating sur-
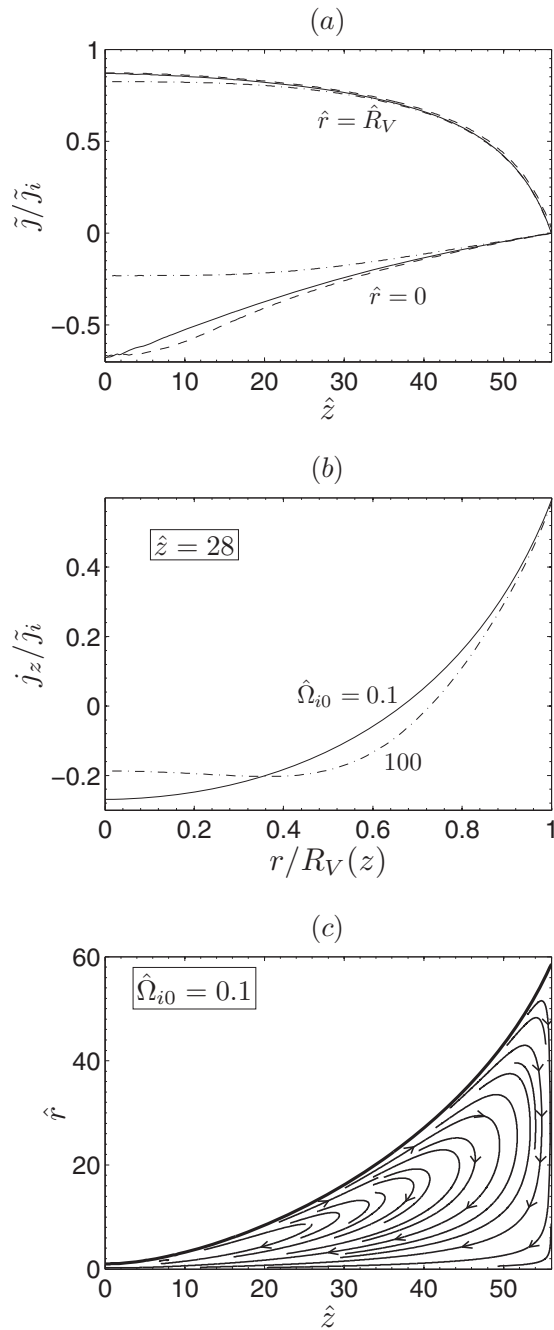
FIG. 8. The same as Fig. 7 except that current ambipolarity, $\tilde{j}=0$, is imposed at the downstream end of integration.

face. In this case, plasma resistivity inside the plasma source would facilitate the closure of the electric current lines there. For a plasma jet expanding into vacuum, the actual condition for $\tilde{j}_z(0,r)$ is uncertain because it needs to couple the solution of the present model with both the downstream detachment model and the upstream plasma source model. The main point here is that the longitudinal electric current density does not affect the plasma acceleration process as long as the induced azimuthal magnetic field is negligible, which is the case with a low-beta plasma.

The development of the ion-electron streamtube separation and the related failure of current ambipolarity questions the detachment model for a low-beta plasma of Hooper,[18]

which takes current ambipolarity as a central assumption. We have shown here that the combination of quasineutrality, a global current-free plasma, and zero currents at the boundaries is not enough to justify current ambipolarity everywhere. Indeed, from the mathematical viewpoint, the exchange of the *scalar* current conservation equation $\nabla \cdot \tilde{j}=0$ (a combination of the ion and electron continuity equations) by the *vectorial* equation $\tilde{j}=0$ leads to an incompatible model, unless another original plasma equation is satisfied automatically (or is ignored).

V. THRUST TRANSMISSION AND PLUME EFFICIENCY

Equations (27) and (28) detail the radial and axial forces driving the plasma, once the ambipolar field has been canceled out. The magnetic force has contributions of different signs from the Hall and swirl currents. Let us consider first the nonuniform jet when the Hall current is dominant. Then, in the radial direction [Eq. (27)] there are the *expanding* pressure gradient and the *confining* magnetic force. These are balanced exactly at the nozzle throat but the pressure gradient tends to dominate downstream, forcing the radial expansion of the plasma. In the axial direction [Eq. (28)] the pressure gradient and the magnetic force constitute the *electrothermal and Hall acceleration* mechanisms, respectively. Since $\alpha(z)$ increases with z, the relative influence of the Hall acceleration increases downstream. In the case of the uniform jet, there is no confining magnetic force from the Hall current; on the contrary, the swirl current leads to a radially expanding and axially decelerating magnetic force.

The *local plasma* thrust is defined as $F(z)=F_i(z)+F_e(z)$, with

$$F_i = 2\pi \int_0^{R_V(z)} drr n m_i u_{zi}^2, \quad F_e = 2\pi \int_0^{R_V(z)} drr n T_e, \quad (40)$$

the momentum/ion and pressure/electron thrusts, respectively. Combining the axial momentum equations of ions and electrons, in order to eliminate the ambipolar electric field, and integrating the resultant equation in a volume $\mathcal{V}(z)$ bounded by the throat, a generic axial cross section downstream the nozzle, and the lateral area $A_V(z)$ of the plasma jet, the local thrust is expressed as

$$F(z) = F_0 + F_s + F_v, \quad (41)$$

with $F_0=F(0)$,

$$F_s = \int_{A_V(z)} dA p_e \sin \alpha, \quad F_v = \int_{\mathcal{V}(z)} d\mathcal{V}(-j_\theta)B_r. \quad (42)$$

For the case of a solid nozzle and a neutral gas, F_0 is the resultant of the gas pressure inside the discharge region, F_s is the pressure of the gas on the wall of the divergent nozzle, and F_v is zero. As is well known, the solid nozzle has two roles: first and principal, the gas pressure on the divergent nozzle walls increments the thrust and, second, the nozzle geometry allows an efficient conversion of pressure thrust (50% of F_0 at the nozzle throat) into momentum thrust for the supersonic plasma. For our plasma thruster configuration, F_0 is mainly an electrothermal contribution;[22] F_v is the

TABLE II. Performance parameters for different combinations of nozzles and plasma jets. In the first column: input parameters are the upper four ones; the rest are output parameters evaluated at $z=z_F$.

R_L/R	5.4	5.4	5.4	5.4	3.5	3.5	3.5
$\hat{\Omega}_{i0}$	0.1	0.1	100	100	100	100	100
σ	0.99	0	0.99	0	0.99	0	0
M_0	1.05	1.05	1.05	1.05	1.05	1.05	1.01
F_0/F	0.49	0.52	0.49	0.53	0.58	0.63	0.63
F_s/F	0.01	0.48	0.01	0.56	0.01	0.52	0.52
F_v/F	0.51	$\simeq 0$	0.50	-0.09	0.41	-0.15	-0.15
$P_{zi,0}/P_{zi}$	0.07	0.08	0.07	0.09	0.11	0.14	0.13
$P_{zi,\mathrm{th}}/P_{zi}$	0.21	0.92	0.23	1.06	0.28	1.15	1.16
$P_{zi,\mathrm{mag}}/P_{zi}$	0.72	$\simeq 0$	0.70	-0.15	0.61	-0.29	-0.29
$P_{i,0}/P_i$	0.06	0.06	0.06	0.06	0.09	0.09	0.08
$P_{i,\mathrm{th}}/P_i$	0.92	0.94	0.93	0.94	0.91	0.91	0.92
$P_{i,\mathrm{mag}}/P_i$	0.02	0	0.01	0	$\simeq 0$	0	0
F_i/F	0.94	0.93	0.94	0.92	0.91	0.89	0.89
η_{plume}	0.83	0.72	0.81	0.69	0.78	0.63	0.63

(volumetric) Hall contribution to thrust and, since the magnetic nozzle has no walls, the thrust mechanism associated with F_s cannot be a pressure force.

In fact, F_s is a second Hall contribution coming from a surface Hall current that develops at the plasma edge, in a thin transition layer matching the bulk plasma jet and the adjacent vacuum. We postulate that the surface Hall current per unit of length along the plasma edge is

$$J_\theta(z) = -\left.(p_e/B)\right|_{[z,R_V(z)]}. \tag{43}$$

Appendix C justifies this result for the simplest magnetic configuration and plasma distribution function. The kinetic solution of the transition layer, of typical length $\delta L = O(2\ell_e)$, shows how the plasma pressure drops to zero and gives rise to a diamagnetic current density, which integrated across the layer yields J_θ. In the limit $\ell_e/R_V \ll 1$ adopted in our model, the transition layer is just a current sheet between plasma and vacuum. The substitution of p_e from Eq. (43) into F_s in Eq. (42) demonstrates that the increment in thrust in the magnetic nozzle comes from surface and volumetric electromagnetic contributions.

Figure 9(a) plots the local thrust function for different simulation cases. In order to compare nozzles with different divergence rates, $\hat{R}_V(\hat{z})$ has been used as abscissa instead of $\hat{z}$. Table II shows the relative weight of the three contributions to thrust for different cases (and the relative contribution of the ion/momentum thrust at the final section, F_i/F). The uniform and nonuniform plasma jets considered here constitute two limit examples of the two thrust mechanisms of the divergent nozzle, F_s and F_v. In the case of the uniform jet, F_s is the main contribution, whereas the plasma swirling caused by $j_{\theta i}$ leads to a negative contribution of F_v, which is a significant penalty when $\hat{\Omega}_{i0}$ is large (and the nozzle is short). The nonuniform jet has $F_s \ll F_v$ because of the low density at the plasma edge, and the positive F_v is driven by the large Hall current, which dominates totally over the swirl current (as indicated by the low influence of $\hat{\Omega}_{i0}$ on the re-

sults). In spite of these important differences, both types of plasma jets provide thrusts of similar magnitude in the same nozzle [Fig. 9(a)].

The equation for the ion axial power (i.e., the axial flow of ion axial energy) is obtained from the axial momentum equation for ions and takes the form

$$P_{zi}(z) = 2\pi \int_0^{R_V(z)} dr\, r n \frac{m_i}{2} u_{zi}^3 = P_{zi,0} + P_{zi,\mathrm{th}} + P_{zi,\mathrm{mag}}, \tag{44}$$

with $P_{zi,0} = P_{zi}(0)$,

$$P_{zi,\mathrm{th}} = -\int_{\mathcal{V}(z)} d\mathcal{V} u_{zi}\frac{\partial p_e}{\partial z}, \quad P_{zi,\mathrm{mag}} = -\int_{\mathcal{V}(z)} d\mathcal{V} u_{zi} j_\theta B_r. \tag{45}$$

Here, $P_{zi,\mathrm{th}}$ and $P_{zi,\mathrm{mag}}$ correspond, respectively, to the electrothermal and electromagnetic power gains based on the works of the respective (volumetric) forces. Table II shows that the magnetic contribution dominates for the nonuniform jet, whereas, for the uniform jet, the electrothermal energy is the dominant contribution and the swirl current contributes negatively. Therefore, a 1D picture based on the balance equation (44) for the axial power would suggest that the magnetic nozzle is predominantly an electrothermal and/or electromagnetic plasma accelerator depending on the initial plasma conditions. The conclusion is subtler when we look at the equation for the total ion power.

The equation for the ion mechanical energy is

$$\nabla \cdot \left(\tfrac{1}{2}m_i u_i^2 n_i \boldsymbol{u}_i\right) = -\boldsymbol{j}_i \cdot \nabla\phi = -\boldsymbol{u}_i \cdot \nabla p_e + \boldsymbol{u}_i \cdot (\boldsymbol{j} \times \boldsymbol{B}). \tag{46}$$

Integrating it in the volume $\mathcal{V}(z)$, the ion total power function satisfies

$$P_i(z) = 2\pi \int_0^{R_V(z)} dr\, r n u_{zi} \frac{m_i}{2} u_i^2 = P_{i,0} + P_{i,e}, \qquad (47)$$

with $P_{i,0} = P_i(0)$ and $P_{i,e}$ the electric work on the ions (along the nozzle). This can be split as $P_{i,e} = P_{i,\text{th}} + P_{i,\text{mag}}$, with

$$P_{i,\text{th}} = -\int_{\mathcal{V}(z)} d\mathcal{V} \boldsymbol{u}_i \cdot \nabla p_e, \quad P_{i,\text{mag}} = \int_{\mathcal{V}(z)} d\mathcal{V} \boldsymbol{u}_i \cdot (\boldsymbol{j}_e \times \boldsymbol{B}) \qquad (48)$$

as the thermal and magnetic works, respectively. The ion power function is plotted in Fig. 9(b), and the internal, electrothermal, and electromagnetic contributions at z_F are detailed in Table II. Interestingly, the net electromagnetic work is very small since it is proportional to the electron-ion streamtube separation: one has $|\boldsymbol{u}_i \cdot (\boldsymbol{j}_e \times \boldsymbol{B})| = |j_{\theta e} B u_i \sin \alpha_{ei}|$. Therefore, the magnetic nozzle acts predominantly as an electrothermal accelerator. The mutual cancellation of the partial magnetic works and the work of the pressure radial gradient explains that $P_{i,\text{mag}} \ll P_{zi,\text{mag}}$.

The radial expansion of the plasma means a plume divergence that affects negatively the efficiency of the plasma thruster. An approximate parameter to measure this effect is the plume efficiency (based on ion properties only), defined as

$$\eta_{\text{plume}}(z) = P_{zi}/P_i \simeq F_i^2/(2\dot{m}_i P_i), \qquad (49)$$

where $\dot{m}_i$ is the ion mass flow and the last near equality has been checked with the simulations. The plume efficiency is one of the factors contributing to the thrust efficiency of the whole thruster. It is plotted in Fig. 9(c) as function of $\hat{z}$.

Figures 9(a)–9(c) illustrate on the aspects influencing the nozzle propulsive performance. The long nozzle has a better propulsive performance than the short one, which means that the long nozzle has a larger focusing effect on the plasma (this is the kind of result that the 1D model does not provide). For a given nozzle, the total kinetic power transmitted to the ions is almost independent of both the nonuniformity and ion-magnetization parameters, σ and $\hat{\Omega}_{i0}$. The axial ion power and the plume efficiency are higher for a nonuniform jet because of the plasma concentration near the axis. Increasing the ion magnetization, which tends to expand radially the ions and to increase the swirl current, has an unfavorable effect on plume efficiency. This indicates that decreasing the guiding field, which means increasing the plasma beta, is favorable for plume efficiency. Winglee et al.[16] pointed out a second benefit: as the plasma beta is increased, self-field detachment is facilitated. This suggests that a moderately low beta at the magnetic throat is optimum for acceleration and detachment.

Finally, we checked that the plasma acceleration response is not affected by the local imprecision at the nozzle throat related to the small parameter $(M_0 - 1)$. The two last columns of Table II show (for the worst simulation case) that results with $M_0 - 1 = 0.05$ and 0.01 are practically identical at the downstream end z_F.

VI. CONCLUSIONS

A 2D model of the supersonic expansion of a collisionless, low-beta, current-free plasma jet in a magnetic nozzle has been analyzed. The main governing parameters are the nozzle/jet divergence rate, the magnetic strength on ions, and the radial nonuniformity of the plasma density at the nozzle throat. Electrons are assumed fully magnetized so that electron streamtubes are magnetic streamtubes. Jets with a uniform density at the throat have zero Hall (electron) current there and the Hall current remains zero since the electron flow conserves its macroscopic azimuthal frequency in a streamtube. Nonuniform densities at the throat are sustained by magnetic confinement based on a Hall current.

The radially averaged plasma profiles agree well with those obtained from a simple 1D model, which indicates that ion magnetization and jet initial nonuniformity have a weak effect on the axial acceleration. There is a relative radial focusing of the jet that mitigates the negative radial expansion effects. Except for fully magnetized ions (an unlikely case in practical applications), ion streamtubes do not coincide with electron/magnetic streamtubes. This separation of streamtubes produces, first, longitudinal electric currents, which indicate that current ambipolarity, used in some nozzle detachment models, is not fulfilled. Second, it allows the creation of a modest swirl current that competes negatively with the Hall current.

For an initially nonuniform jet, the driving radial forces are the expanding pressure and the confining magnetic force; axially, the plasma is accelerated by electrothermal and electromagnetic (mainly Hall) forces. The thrust and energy analysis stands out the dual character of the magnetic nozzle: it is an electromagnetic device from the thrust viewpoint and mostly an electrothermal device from the viewpoint of ion energy gain. Indeed, the contribution of electromagnetic work to the ion power is due to the lack of current ambipolarity.

A more detailed analysis of the thrust mechanisms on the magnetic nozzle unveils basic differences with those in a solid nozzle. In the magnetic nozzle, the role of the pressure on the walls of the solid nozzle is taken up by a Hall current layer, of a thickness of few electron gyroradii, developing at the plasma/vacuum interface. In general, the thrust adds the contributions of the volumetric and surface Hall currents. Plume efficiency, a factor contributing to the thrust efficiency, is found to be larger for a long nozzle, a highly nonuniform jet, and weak ion magnetization. This result and some considerations on detachment suggest that the optimum magnetic field is such that the plasma beta at the throat be moderately small.

The present model admits rather straightforward extensions to plasmas with more elaborate models of the ion and electron thermodynamics. The case of an ion population with a high, anisotropic internal energy would be relevant to the VASIMR.[6] The case of a plasma with two electron populations of disparate temperatures would extend the 1D analysis of Ahedo and Martínez-Sánchez[14,15] on electric potential steepening, allowing an assessment of the 2D shape of a current-free double layer.
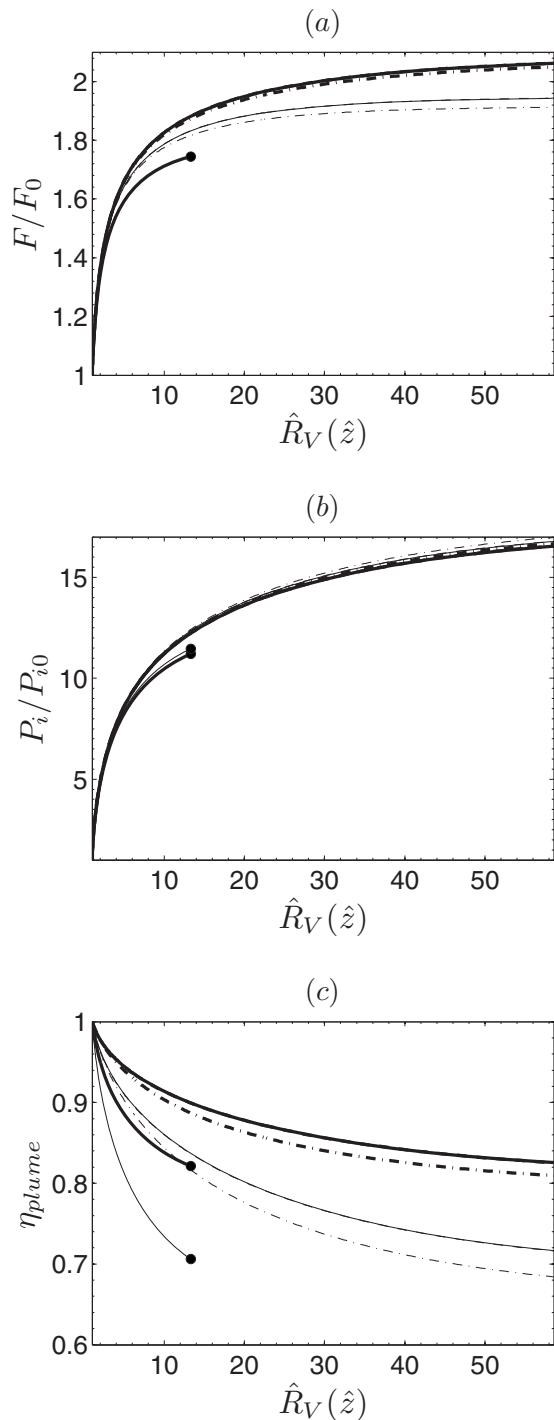
FIG. 9. Variation along the nozzle of (a) thrust, (b) ion energy flow, and (c) plume efficiency; $F_0=F(0)$ and $P_{i0}=P_i(0)$ correspond to throat conditions of the upstream plasma. Thin and thick lines are for the uniform and nonuniform ($\sigma=0.99$) jets, respectively. Magnetic strengths are $\hat{\Omega}_{i0}=0.1$ (solid), 10 (dashed), and 100 (dashed-dotted). Results are for a long nozzle except those curves ending with a black circle, which are for the short nozzle.

The main limitations of our model are at its upstream and downstream boundaries. First, since the model assumes fully magnetized electrons, zero resistivity, and no induced magnetic field, the simulation of any detachment process and its effect on nozzle performances is not possible. Nonetheless, a first assessment of the different detachment mechanisms can be made from the results of the present model.[24]

Second, the coupling with the upstream plasma source would allow one to clarify the plasma transonic conditions at the throat (but the integration of this subsonic/supersonic model would require to use a different numerical technique). Finally, the coupling with the upstream and downstream regions would allow one to determine, without uncertainty, the electron current density and the closure of the electric current lines.

ACKNOWLEDGMENTS

APPENDIX A: METHOD OF CHARACTERISTICS

The method of characteristics[27] is used to integrate numerically Eqs. (26)–(28). The ion streamlines, $C_i : r = r_i(z)$, with $dr_i/dz = \lambda_i = u_{ri}/u_{zi}$, constitute the first family of characteristic curves. The evolution equation along the ion streamlines is

$$u_{zi} \left.\frac{du_{zi}}{dz}\right|_{C_i} + u_{ri} \left.\frac{du_{ri}}{dz}\right|_{C_i} + c_s^2 \left.\frac{d\ln n}{dz}\right|_{C_i}$$
$$= (u_{\theta i} - u_{\theta e})\Omega_i(\lambda_i \cos\alpha - \sin\alpha) + \lambda_i \frac{u_{\theta i}^2}{r}. \quad \text{(A1)}$$

Then, there are the two families of ion Mach lines, $C_\pm : r = r_\pm(z)$, with

$$\frac{dr_\pm}{dz} = \lambda_\pm = \frac{u_{zi}u_{ri} \pm c_s\sqrt{u_{zi}^2 + u_{ri}^2 - c_s^2}}{u_{zi}^2 - c_s^2}. \quad \text{(A2)}$$

The evolution equations along these two characteristic families are

$$u_{zi} \left.\frac{du_{ri}}{dz}\right|_{C_\pm} - u_{ri} \left.\frac{du_{zi}}{dz}\right|_{C_\pm} \pm c_s\sqrt{u_{zi}^2 + u_{ri}^2 - c_s^2} \left.\frac{d\ln n}{dz}\right|_{C_\pm}$$
$$= (u_{ri} - \lambda_\pm u_{zi})\frac{u_{ri}}{r} + \frac{u_{\theta i}^2}{r} + (u_{\theta i} - u_{\theta e})\Omega_i$$
$$\times(\cos\alpha + \lambda_\pm \sin\alpha). \quad \text{(A3)}$$

Observe that plasma equations present removable singularities at $r=0$, where u_{ri}, $u_{\theta i}$, and $u_{\theta e}$ are zero. For instance, the Taylor expansion of Eq. (20) yields, at $r=0$,

$$2m_i u_{\theta i}/r \rightarrow n u_{zi}(dD_i/d\psi_i) - eB_z. \quad \text{(A4)}$$

Either the plasma equations must be regularized before integration or the numerical scheme must deal correctly with them. Following Zucrow and Hoffman,[27] the second option has been adopted here.

The accuracy of the integration scheme is evaluated by checking the conservation of the ion mechanical energy along the ion streamlines [Eq. (17)]. The axial ion angular momentum along the ion streamlines is automatically conserved when determining $u_{\theta i}$ from Eq. (20).

APPENDIX B: STRUCTURE OF A MAGNETIZED CYLINDRICAL PLASMA

Recently, Ahedo[28] carried out a detailed study of the radial structure of a plasma confined by a long dielectric cylindrical vessel of radius R and an axial magnetic field of strength B_0. The main distinguished magnetized regime corresponds to

$$\Omega_{lh0} \gg c_s/R, \nu_e, \tag{B1}$$

with ν_e as the effective electron collisionality and $\Omega_{lh0} = \Omega_{i0}\sqrt{m_i/m_e}$ as the lower-hybrid frequency. In that regime, the radial structure of the plasma consists of a bulk diffusive region and two thin layers: a quasineutral convective layer and the Debye sheath. The layer thicknesses are the local electron gyroradius ℓ_e^* and the local Debye length λ_d, respectively, and the hierarchy $\lambda_d \ll \ell_e^* \ll R$ is assumed. The plasma behavior in the bulk diffusive region is summarized next. First, electron pressure is balanced by the radial magnetic force,

$$-en\frac{\partial \phi}{\partial r} \ll enu_{\theta e}B_0 \simeq -T_e\frac{\partial n}{\partial r}. \tag{B2}$$

Second, since the electric force is very small, the plasma radial velocity is very small. Third, the swirl current is negligible compared to the Hall current. Fourth, the electron azimuthal velocity satisfies

$$u_{\theta e} \simeq u_r\Omega_{e0}/\nu_e, \tag{B3}$$

with Ω_{e0} as the electron gyrofrequency. Fifth, the ion continuity equation and the above equations determine the radial structure, characterized by

$$n(r) = n_0 J_0\left(a_0\frac{r}{R}\right), \quad -j_{\theta e}(r) \equiv enu_{\theta e} = \frac{n_0 T_e}{B_0 R}a_0 J_1\left(a_0\frac{r}{R}\right), \tag{B4}$$

with J_0 and J_1 as Bessel functions of the first kind and $a_0 \simeq 2.405$ is the first zero of J_0. Fifth, the transition to the thin inertial layer takes place when $u_{\theta e}$ is, roughly, of the order of the electron thermal velocity, $c_e = \sqrt{T_e/m_e}$. From $u_{\theta e} \sim c_e$ and Eq. (B4), a (crude) estimate of the transition location is

$$R - r \sim c_s/\Omega_{lh0}. \tag{B5}$$

Observe in Eq. (B4) that $|\hat{j}_{\theta e}|$ decreases as B_0 increases. The reason is that, within the magnetized regime, the plasma density near the wall decreases as magnetic confinement increases, whereas $u_{\theta e}/c_e$ changes weakly.
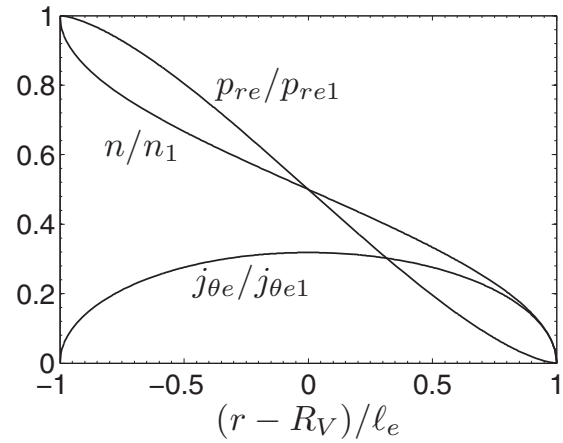

FIG. 10. Variation in plasma magnitudes in the current sheet separating the bulk region from the vacuum, for a parallel, uniform jet.

The solution of the bulk region for a strongly magnetized, cylindrical plasma is used in Sec. II D to define the nozzle entrance conditions (31)–(35). In order to ignore the two thin layers and to cover different radial gradients of the plasma density, the parameter σ is defined. For a highly nonuniform jet, the value of σ is based on Eq. (B5).

APPENDIX C: THE PLASMA-VACUUM EDGE

Let us consider a cylindrical plasma jet in an axial magnetic field B. Electrons constitute a monoenergetic population of velocities $v_{\perp 1}$ and $v_{\parallel 1}$, perpendicular and parallel to the magnetic field, respectively. The distribution of electron gyrocenters is uniform for $0 \leq r \leq R_V$ and zero otherwise. Since the electron gyroradius is $\ell_e = m_e v_{\perp 1}/eB$, the plasma density is constant (n_1 say) in the region $0 \leq r \leq R_V - \ell_e$ and decreases to zero in the transition layer $R_V - \ell_e \leq r \leq R_V + \ell_e$. Ions are assumed unmagnetized and provide quasineutrality everywhere. Clearly, the macroscopic plasma velocity reduces to $u_{\parallel 1} = v_{\parallel 1}$.

The local plasma density, Hall current density, and (radial) pressure in that layer are obtained, respectively, from

$$n(r) = \int d^3\mathbf{v}f_e,$$

$$j_{\theta e}(r) = -e\int d^3\mathbf{v}f_e v_\theta, \tag{C1}$$

$$p_{re}(r) = m_e\int d^3\mathbf{v}f_e v_r^2,$$

where the local distribution function $f_e(r,\mathbf{v})$ is obtained from the distribution of gyrocenters. Let φ be the velocity phase angle defined from $v_r = v_\perp \sin\varphi$ and $v_\theta = v_\perp \cos\varphi$. For r within the transition layer, the range of φ where electrons exist is

$$|\varphi| \leq \varphi_l(r) = \arccos(r - R_V)/\ell_e, \tag{C2}$$

with $\varphi_l(R_V - \ell_e) = \pi$ and $\varphi_l(R_V + \ell_e) = 0$. Then, the integrations on $\mathbf{v}$ in Eq. (C1) are immediate, yielding

$$n_e(r) = \frac{n_1}{\pi}\varphi_l,$$

$$j_{\theta e}(r) = \frac{j_{\theta e1}}{\pi}\sin\varphi_l, \tag{C3}$$

$$p_{re}(r) = \frac{p_{re1}}{\pi}[\varphi_l - \sin\varphi_l\cos\varphi_l],$$

with $j_{\theta e1} = -en_1 v_{\perp 1}$ and $p_{re1} = m_e n_{e1} v_{\perp 1}^2/2$. These expressions are plotted in Fig. 10. They verify the macroscopic equation

$$0 = -\frac{\partial p_{re}}{\partial r} + j_{\theta e}B, \tag{C4}$$

so that the Hall current is the diamagnetic current created by the pressure gradient, and peaks at $r = R_V$. The integration of this last equation across the layer yields the diamagnetic current per length postulated in Eq. (43),

$$J_\theta = \int_{R_V-\ell_e}^{R_V+\ell_e} j_{\theta e}\,dr = -\frac{1}{B}p_{re}(R_V - \ell_e). \tag{C5}$$

[1] A. Sasoh and Y. Arakawa, J. Propul. Power **8**, 98 (1992).
[2] G. Krülle, M. Auweter-Kurtz, and A. Sasoh, J. Propul. Power **14**, 754 (1998).
[3] C. Charles and R. Boswell, Appl. Phys. Lett. **82**, 1356 (2003).
[4] S. A. Cohen, X. Sun, N. Ferraro, E. E. Scime, M. Miah, S. Stange, N. Siefert, and R. Boivin, IEEE Trans. Plasma Sci. **34**, 792 (2006).
[5] O. Batishchev, IEEE Trans. Plasma Sci. **37**, 1563 (2009).
[6] A. Arefiev and B. Breizman, Phys. Plasmas **11**, 2942 (2004).
[7] D. Courtney and M. Martínez-Sánchez, *Proceedings of the 30th International Electric Propulsion Conference*, Florence, Italy (Electric Rocket Propulsion Society, Fairview Park, OH, 2007), Paper No. IEPC-2007-39.
[8] R. Hoyt, J. Scheuer, K. Schoenberg, R. Gerwin, R. Moses, and I. Henins, IEEE Trans. Plasma Sci. **23**, 481 (1995).
[9] K. Schoenberg, R. Gerwin, R. Moses, J. Scheuer, and H. Wagner, Phys. Plasmas **5**, 2090 (1998).
[10] M. J. Hole and S. W. Simpson, Phys. Plasmas **4**, 3493 (1997).
[11] S. A. Andersen, V. O. Jensen, P. Nielsen, and N. D'Angelo, Phys. Fluids **12**, 557 (1969).
[12] M. Inutake, A. Ando, K. Hattori, H. Tobari, and T. Yagai, J. Plasma Fusion Res. **78**, 1352 (2002).
[13] A. Sasoh, Phys. Plasmas **1**, 464 (1994).
[14] E. Ahedo and M. Martínez-Sánchez, "The role of current-free double-layers in plasma propulsion," AIAA Paper No. 2008-5005, 2008.
[15] E. Ahedo and M. Martínez-Sánchez, Phys. Rev. Lett. **103**, 135002 (2009).
[16] R. Winglee, T. Ziemba, L. Giersch, J. Prager, J. Carscadden, and B. R. Roberson, Phys. Plasmas **14**, 063501 (2007).
[17] R. W. Moses, R. Gerwin, and K. Schoenberg, AIP Conf. Proc. **246**, 1293 (1992).
[18] E. B. Hooper, J. Propul. Power **9**, 757 (1993).
[19] A. Arefiev and B. Breizman, Phys. Plasmas **12**, 043504 (2005).
[20] C. A. Deline, R. D. Bengtson, B. N. Breizman, M. R. Tushentsov, J. E. Jones, D. G. Chavers, C. C. Dobson, and B. M. Schuettpelz, Phys. Plasmas **16**, 033502 (2009).
[21] D. P. F. Ferri, D. Manente, D. Curreli, Y. Guclu, D. Melazzi, D. Rondini, S. Suman, J. Carlsson, C. Bramanti, E. Ahedo, V. Lancellotti, K. Katsonis, and G. Markelov, *Proceedings of the 31th International Electric Propulsion Conference*, Ann Arbor, MI (Electric Rocket Propulsion Society, Fairview Park, OH, 2009), Paper No. IEPC 2009-205.
[22] E. Ahedo, *Proceedings of the 31st International Electric Propulsion Conference*, Ann Arbor, MI (Electric Rocket Propulsion Society, Fairview Park, OH, 2009), Paper No. IEPC 2009-193.
[23] E. Ahedo and M. Merino, "Two-dimensional plasma acceleration in a divergent magnetic nozzle," AIAA Paper No. 2009-5361, 2009.
[24] E. Ahedo and M. Merino, *Proceedings of the 31st International Electric Propulsion Conference*, Ann Arbor, MI (Electric Rocket Propulsion Society, Fairview Park, OH, 2009), Paper No. IEPC 2009-002.
[25] J. Jackson, *Classical Electrodynamics* (Wiley, New York, 1999).
[26] M. Abramowitz and I. Stegun, *Handbook of Mathematical Functions* (Dover, New York, 1965).
[27] M. Zucrow and J. Hoffman, *Gas Dynamics* (Wiley, New York, 1976).
[28] E. Ahedo, Phys. Plasmas **16**, 113503 (2009).
[29] M. Merino, "Toberas Magnéticas para Motores Espaciales de Plasma," Engineer Degree thesis, Universidad Politécnica de Madrid (available at http://web.fmetsia.upm.es/ep2/), 2010.